



# Highly efficient photo-Fenton degradation of methyl orange facilitated by slow light effect and hierarchical porous structure of $\text{Fe}_2\text{O}_3\text{-SiO}_2$ photonic crystals



Liang Zhou<sup>a</sup>, Juying Lei<sup>a,\*\*\*</sup>, Lingzhi Wang<sup>b</sup>, Yongdi Liu<sup>a,\*\*\*</sup>, Jinlong Zhang<sup>b,c,\*</sup>

<sup>a</sup> State Environmental Protection Key Laboratory of Environmental Risk Assessment and Control on Chemical Process, School of Resources and Environmental Engineering, East China University of Science and Technology, 130 Meilong Road, Shanghai 200237, PR China

<sup>b</sup> Key Lab for Advanced Materials and Institute of Fine Chemicals, East China University of Science and Technology, 130 Meilong Road, Shanghai 200237, PR China

<sup>c</sup> Suzhou Jukang New Materials Co. Ltd of Science and Technology, 558 Fenhu Road, Suzhou 212111, PR China

## ARTICLE INFO

### Keywords:

Hierarchical macro-mesoporous  
 $\text{Fe}_2\text{O}_3\text{-SiO}_2$  photonic crystal  
Slow light effect  
 $\text{H}_2\text{O}_2$   
Photo-Fenton

## ABSTRACT

In this work, the  $\text{Fe}_2\text{O}_3\text{-SiO}_2$  composite photo-Fenton catalyst was designed and synthesized as a photonic crystal with a hierarchical macro-mesoporous structure, which possesses a slow-light-effect region that overlaps with the absorption spectrum of methyl orange (MO). The prepared material exhibits remarkably high and stable photo-Fenton catalytic performance for the degradation of MO using only a low concentration of  $\text{H}_2\text{O}_2$  under visible light irradiation. The catalytic activity of the as-prepared material is better than that of the corresponding macroporous or mesoporous  $\text{Fe}_2\text{O}_3\text{-SiO}_2$  composites as well as commercial  $\text{Fe}_2\text{O}_3$  or the homogenous photo-Fenton system of  $\text{FeCl}_3 \cdot 6\text{H}_2\text{O}$ . The efficient use of  $\text{H}_2\text{O}_2$  and the high catalytic activity are attributed to (i) the excellent adsorption of MO by the hierarchical macro-mesoporous structure and (ii) enhanced light harvesting from coupling the absorption spectrum of MO with the slow-light-effect region of the photonic crystal. This hierarchical macro-mesoporous  $\text{Fe}_2\text{O}_3\text{-SiO}_2$  photonic crystal is expected to be a promising cost-effective photo-Fenton catalyst for degradation of a variety of dyes by deliberately tuning its slow-light-effect region, and opens up new perspectives for the development of highly efficient photo-Fenton catalysts for environmental remediation technology.

## 1. Introduction

Leftover organic dyes dissolved in water are considered refractory industrial waste, solutions of which are intensely colored, highly toxic and exhibit poor biodegradability [1]. With the increasing use of synthetic dyes in a variety of industries, the treatment of organic dye waste water before their release has been promoted as one way to protect the environment from the detrimental effects of these dyes [2,3]. However, since conventional biological wastewater treatment processes are not efficient at removing most of these dyes [4,5], the treatment of dye wastewater has proven rather difficult. The development of cost-effective methods to remove dyes from wastewater is urgently needed.

Advanced oxidation processes (AOPs) are considered promising methods for the treatment of toxic organic pollutants in industrial wastewater [6–9]. Among a variety of AOPs, Fenton's reagent has attracted much attention due to its strong oxidation potential, mild

reaction conditions and easy operation. Even more promising, light irradiation can further enhance the catalytic activity of the system, a reaction called the photo-Fenton process. Unfortunately, the drawbacks associated with the homogeneous Fenton or photo-Fenton process, namely easy deactivation by ion-complexing agents like phosphate anions and the formation of large amounts of iron-containing sludge, limit the application of this reaction [10–12]. Therefore, many efforts have been made to incorporate heterogeneously photo-Fenton catalysts into various supports, such as crushed brick, activated alumina, zeolite, silica, graphene oxide, etc [13–17]. However, the resulting supported catalysts are more or less unsatisfactory in terms of their relatively low efficiencies of hydrogen peroxide utilization [18], or having low specific surface area [19]. Moreover, little has been reported on improving the photo-Fenton catalytic activity by enhancing light-harvesting efficiency, a property determined by the nanostructure of the catalyst.

Recently, photonic crystals have become an attractive topic in part

\* Corresponding author at: State Environmental Protection Key Laboratory of Environmental Risk Assessment and Control on Chemical Process, East China University of Science and Technology, 130 Meilong Road, Shanghai 200237, PR China.

\*\* Corresponding authors.

E-mail addresses: [leijuying@ecust.edu.cn](mailto:leijuying@ecust.edu.cn) (J. Lei), [ydliu@ecust.edu.cn](mailto:ydliu@ecust.edu.cn) (Y. Liu), [jlzhang@ecust.edu.cn](mailto:jlzhang@ecust.edu.cn) (J. Zhang).

because of their potential applications [20,21]. Photonic crystals (PCs) with ordered macroporous structures give rise to the photonic stop band for certain frequencies of light [22]. Photons near photonic stop band edges can be slowed down (termed slow photons). If the energy of slow photons overlaps with the absorbance of the material or dye interest, its absorption can be enhanced as a result of the increased effective optical path length [22,23]. Therefore, a photo-Fenton catalyst with a PC structure can promote light harvesting for the photo-Fenton reaction and is expected to enhance catalytic activity. Furthermore, incorporating a mesoporous structure into PC framework would effectively increase the specific surface area. Hence, a PC containing a mesoporous framework with 3D ordered macropores is desirable for photo-Fenton catalysis, because creating such a structure will combine high surface area with efficient light harvesting.

Herein, we describe the preparation of a hierarchical macro-mesoporous  $\text{Fe}_2\text{O}_3\text{-SiO}_2$  photonic crystal (MM-Fe-Si-PC) using a double-templated synthesis combining colloidal crystals and an amphiphilic triblock copolymer. The structure of the catalyst was characterized in detail by SEM, TEM, XRD and so on. The photo-Fenton catalytic activity was evaluated by the degradation of methyl orange (MO), a typical azo dye, under visible light irradiation. MO was chosen, because its light absorption spectrum overlaps with the slow-light-effect region of the photonic crystal structure. The photo-Fenton experiments demonstrate that, at a concentration of  $\text{H}_2\text{O}_2$  lower than 0.4 mM, the MM-Fe-Si-PC exhibits remarkable catalytic activity which is better than that of the corresponding mesoporous or macroporous material as well as the commercial  $\text{Fe}_2\text{O}_3$  or the homogeneous Fenton system. The photo-Fenton catalytic mechanism is discussed. Based on a dye-sensitization mechanism, both the excellent adsorption of MO onto the hierarchical macro-mesoporous structure and the enhanced light harvesting from the slow-light effect contribute to the efficient use of  $\text{H}_2\text{O}_2$  and the high catalytic activity. In addition, the photo-Fenton experiments using MM-Fe-Si-PC with different slow-light-effect region for degradation of different dyes demonstrated that the catalyst can be efficient for degradation of a variety of dyes by deliberately tuning the slow-light-effect region to overlap with the light absorption of the dyes. Finally, the stability and reusability of the catalyst were investigated.

## 2. Experimental

### 2.1. Catalyst synthesis

Monodispersed polystyrene (PS) spheres and the PS colloidal crystals were synthesized as described previously [24–26]. For the preparation of MM-Fe-Si-PC, 2.2 mL tetraethylorthosilicate (TEOS) and 2.5 mg acetylacetone (AcAc) were mixed together for 30 min. At the same time, 1.0 g F127, 0.1 mL HCl (2 M) and 0.8 mL deionized water were dissolved in 16 mL of ethanol at 40 °C. After stirring at 25 °C for 1 h, 0.27 g (0.54 g, or 0.81 g)  $\text{FeCl}_3\text{-6H}_2\text{O}$  was added, and then the mixture was continuously stirred until the solution was clear. The mixtures of TEOS and AcAc were then added, and the resulting mixture was continuously stirred at 60 °C for 1 h. The molar ratios of Si/Fe were 200/(10, 20 and 30). Afterwards the PS photonic crystals were immersed into the mesoporous precursor solution. The samples were left air-dry overnight at 25 °C, and were then calcined under the flow of air to remove the templates. The calcination temperature was increased from 25 to 500 °C with a ramp of 2 °C/min and maintained at 500 °C for 4 h. For comparison, macro- and mesoporous structured samples were synthesized according to the above procedure without F127 or PS photonic-crystal templates. These two samples were labeled as Ma-Fe-Si-PC and Me-Fe-Si, respectively. It is worth noting that, we used the 355 nm PS spheres as the template to prepare the above samples which have PC structure. In addition, the hierarchical macro-mesoporous  $\text{Fe}_2\text{O}_3\text{-SiO}_2$  photonic crystal samples using 265 nm and 450 nm PS spheres as the template were prepared for control experiments, and are referred to as MM-Fe-Si-PC-265 and MM-Fe-Si-PC-450. The pure  $\text{SiO}_2$

photonic crystal was labeled as MM-Si-PC by the same method in the absence of  $\text{FeCl}_3\text{-6H}_2\text{O}$ .

### 2.2. Photo-Fenton procedures

For the photo-Fenton degradation experiments, MO (20 mg) was added to 1 L of distilled water adjusted to pH 3.0 using HCl. We took the same steps to prepare the 10 mg/L of Methyl blue (MB) solution and 200 mg/L of 3-formyl-4-methyl-7-hydroxyl coumarin (Coumarin) solution. A 120-mL Quartz glass tube (3.0 cm diameter and 20 cm high) was used as reactor. The catalyst (100 mg) was added to the aqueous solution of MO (100 mL, 20 mg/L, pH = 3.0) in the reactor with vigorous magnetic stirring for half an hour in the dark. Different amounts of  $\text{H}_2\text{O}_2$  were added into the reactor while exposed to light. The light source was a 1000 W tungsten-halide lamp (Philips) equipped with wavelength cutoff filters ( $\lambda > 420$  nm), and the lamp was focused on the reactor. Suitable control experiments (solely  $\text{H}_2\text{O}_2$ , or solely light) were performed under similar conditions in order to provide evidence for the photo-Fenton mechanism in the degradation of MO. In the comparison experiments, the doses used for  $\text{FeCl}_3\text{-6H}_2\text{O}$  in the homogeneous photo-Fenton reaction and commercial  $\text{Fe}_2\text{O}_3$  for the heterogeneous photo-Fenton reaction were calculated according to Eq. (1):

$$\text{Mass (mg)} = \frac{\omega_1\%}{\omega_2\%} \times 100 \quad (1)$$

where  $\omega_1$  is the mass fraction of elemental iron in MM-Fe-Si-PC (data from EDS analysis) and  $\omega_2$  is the mass fraction of elemental iron in commercial  $\text{Fe}_2\text{O}_3$  or  $\text{FeCl}_3\text{-6H}_2\text{O}$ . The percentage of degradation efficiency was calculated using Eq. (2) :

$$\text{Degradation efficiency} = \frac{A_i - A_t}{A_i} \times 100 \quad (2)$$

where  $A_i$  is the initial absorption of the sample, and  $A_t$  is the absorbance at time  $t$ .

### 2.3. Hydroxyl radical determination

The relative number of hydroxyl radicals was detected using a benzoic acid solution. The catalyst (0.1 g) was mixed with 100 mL of benzoic acid (4 mM), MO (20 mg/L), and hydrogen peroxide (0.4 mM) solution. The mixture was irradiated under visible light (1000 W tungsten-halide lamp). The solution was filtered and the filtrate was studied by PL emission spectroscopy to indirectly measure the amount of  $\cdot\text{OH}$  produced (excitation wavelength: 320 nm).

## 3. Results and discussion

### 3.1. Fabrication and structural properties of MM-Fe-Si-PC

To obtain the macro-mesoporous  $\text{Fe}_2\text{O}_3\text{-SiO}_2$  photonic crystals (MM-Fe-Si-PC), monodispersed polystyrene spheres (PS) were used as the template for the assembly of colloidal crystals with 3D-ordered macropores, while the amphiphilic triblock copolymer F127 acted as the template for the mesopores. Fig. 1a shows the uniformly sized and closely arranged PS colloidal crystals. A simple soaking method was used to allow the infiltration of the mixed aqueous solution of silica precursor TEOS, iron precursor  $\text{FeCl}_3\text{-6H}_2\text{O}$  and the amphiphilic triblock copolymer F127 into the voids of the PS colloidal crystal template. The soluble inorganic species and the triblock copolymer combined to form mesostructured hybrid intermediates within these void spaces. After calcinations to remove the PS and triblock copolymer templates, the hierarchical macro/mesoporous MM-Fe-Si-PC was obtained. The content of Fe in the sample was easily controlled by simply adjusting the amount of  $\text{FeCl}_3\text{-6H}_2\text{O}$  and TEOS added during the preparation. The optimal Fe content was determined to be 7.6 wt% by comparing the photo-Fenton catalytic activities of samples with

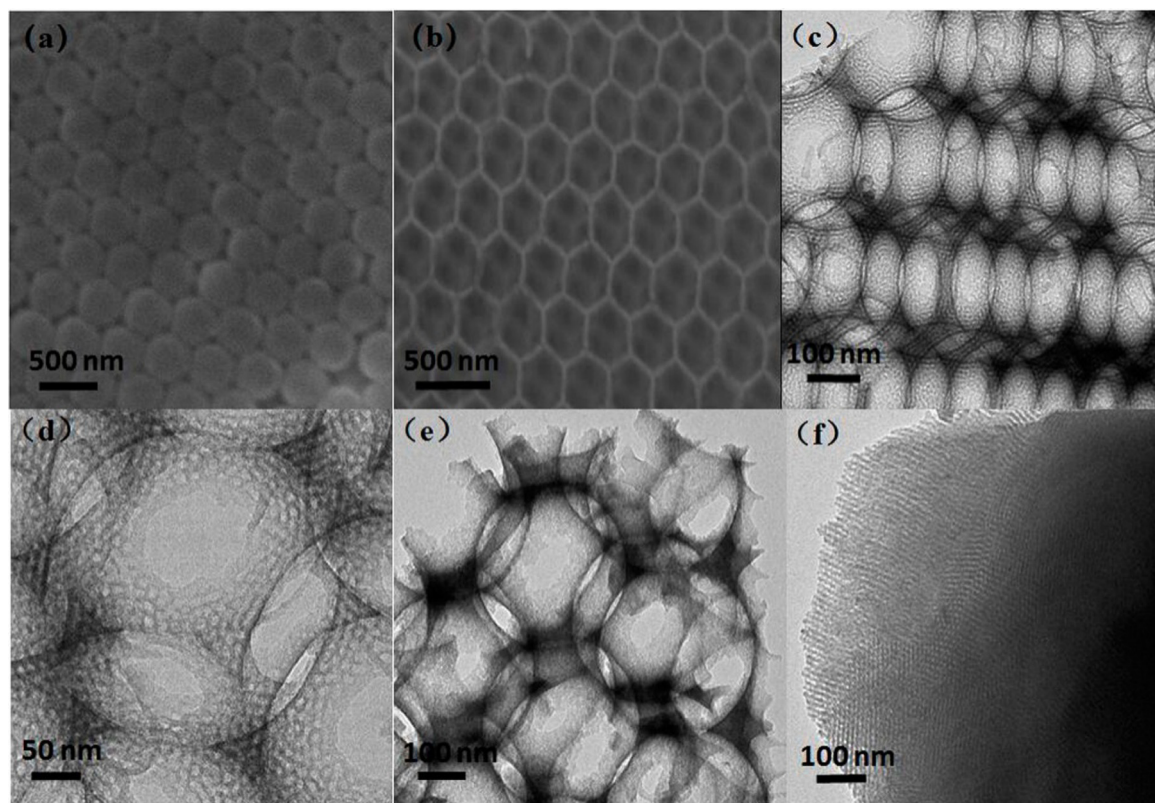


Fig. 1. (a) SEM images of the colloidal crystal template self-assembled from PS spheres; (b, c, d) Typical SEM, TEM and HRTEM images of MM-Fe-Si-PC; (e) TEM image of Ma-Fe-Si-PC; (f) TEM image of Me-Fe-Si.

different Fe content, for which the details can be found in Fig. S1. The MM-Fe-Si-PC sample with 7.6 wt% of Fe content was chosen for the subsequent characterizations and experiments based on its better catalytic performance which is shown in Fig. S2.

The microstructure of the representative MM-Fe-Si-PC sample with 7.6 wt% of Fe was investigated by SEM and TEM. Fig. 1b presents the SEM image of MM-Fe-Si-PC, and shows that 3D ordered and periodic macroporous structures are formed, inheriting the ordered structure of the templating PS colloidal crystals. TEM (Fig. 1c) and HR-TEM images (Fig. 1d) reveal that the wall of the macropores consists of abundant mesopores. In contrast, obvious mesopores inside the macropore walls for the Ma-Fe-Si-PC sample are not observed (Fig. 1e). The BET result of MM-Fe-Si-PC (Fig. S3) is consistent with the TEM results. The  $N_2$  sorption isotherms display a typical type IV isotherm with pronounced  $H_2$  hysteresis loops in the range of  $P/P_0 = 0.4\text{--}0.8$ , indicating the presence of mesopores [27]. The MM-Fe-Si-PC sample also displays high adsorption capacities at high relative pressures ( $P/P_0 > 0.8$ ), an observation which provides evidence for the coexistence of macro and mesopores [28]. The BJH pore size distribution reveals that the majority of mesopores have pore sizes between 2 and 7 nm. The HR-TEM of MM-Fe-Si-PC (Fig. 1d), provides an image that suggests the mesopores within the macropore wall are random, an observation which is quite different from the mesoporous sample (Me-Fe-Si) prepared without the use of PS colloidal crystal templates (Fig. 1f). The mesoporous sample has long range ordered mesopores. Unfortunately, these samples are not the most efficient photocatalysts presumably due to the lack of access of the dye molecules at the surface to the pores. However, there are large differences in the formation of the mesostructures within the regular, confined voids of the PS colloidal crystal. The confined space constrains the interaction between surfactants and the hydrophilic surfaces of PS spheres. As a result, the preferred contact of the substrate surface with the surfactants is disturbed, which not only shortens the pore channel length, but also results in their random

orientation. This disorder leads to a significant increase in pore openings that lead to the surface of the catalyst and improves the accessibility of diffusing species to the mesopores. The optical properties of the sample was measured by UV-vis spectrophotometer with an integrating sphere assembly, using  $\text{BaSO}_4$  as a reflectance sample. As shown in Fig. S4, MM-Fe-Si-PC shows a broad absorption peak between 440 and 800 nm. Compared with the MM-Si-PC sample without  $\text{Fe}_2\text{O}_3$  and the Ma-Fe-Si-PC sample without mesopores, MM-Fe-Si-PC has much stronger absorption in the visible light region, indicating the introduction of  $\text{Fe}_2\text{O}_3$  as well as mesopores in the framework of the silica PC greatly influences its optical properties, and the hierarchical porous structure is more conductive to the absorption of light.

The wide angle XRD pattern of MM-Fe-Si-PC is shown in Fig. 2a. The crystallite corresponds to  $\beta\text{-Fe}_2\text{O}_3$  (JCPDS card No. 39-0238), as evidenced by the strong diffraction peak from the (222) and (440) planes at  $33.0^\circ$  and  $55.2^\circ$ , respectively. Fig. 2b gives the FTIR spectra of MM-Fe-Si-PC. The catalyst exhibits a distinct broad band in the range of  $3100\text{--}3700\text{ cm}^{-1}$ , which accounts for both surface bonded OH stretching of water (present as  $\text{H-OH}$ ) and silanols (present as  $\text{Si-OH}$ ). The low band near  $1640\text{ cm}^{-1}$  is associated with the bending mode of OH groups, which can interact through hydrogen bonds with silanol groups. The absorption band at  $1100\text{ cm}^{-1}$  corresponds to asymmetric stretching vibrations of  $\text{Si-O-Si}$  bonds. The typical peak around  $810\text{ cm}^{-1}$  belongs to the symmetric stretching vibration of  $\text{Si-O-Si}$  bonds. The bands between  $700$  and  $400\text{ cm}^{-1}$  are ascribed to the stretching vibration of  $\text{Fe-O}$  [29], and the peaks at  $620$  and  $456\text{ cm}^{-1}$  are assigned to  $\beta\text{-Fe}_2\text{O}_3$  [30]. These results further confirm that the skeleton of MM-Fe-Si-PC is composed of  $\text{SiO}_2$  and  $\beta\text{-Fe}_2\text{O}_3$ . In addition, the elemental chemical status was determined by XPS. As shown in Fig. S5a, the peaks at  $711.9$  and  $725.4\text{ eV}$  correspond to  $\text{Fe}2\text{p}_{3/2}$  and  $\text{Fe}2\text{p}_{1/2}$ . The  $\text{O}1\text{ s}$  spectrum shown in Fig. S5b can be deconvoluted into three peaks at  $529.2$ ,  $531.6$  and  $532.9\text{ eV}$ , which can be assigned to the oxygen bond of  $\text{H-O-H}$ ,  $\text{Fe-O-H}$  and  $\text{Fe-O}$ , respectively [31,32]. And

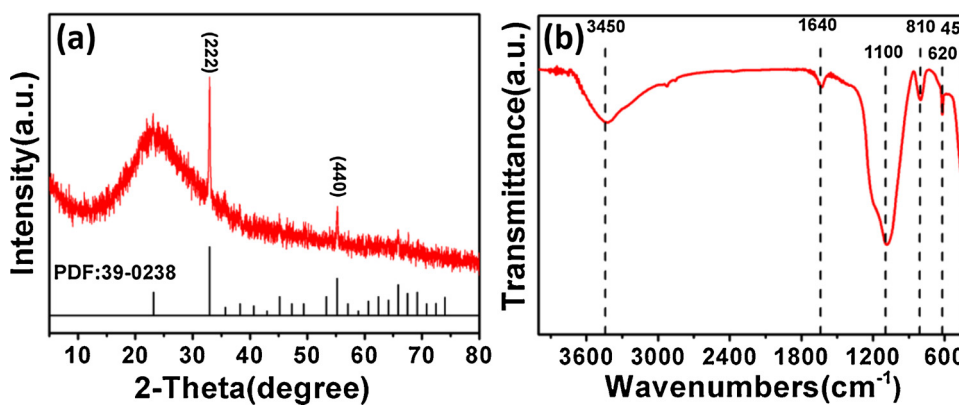


Fig. 2. (a) XRD and (b) FTIR patterns of MM-Fe-Si-PC sample.

the Si 2p spectrum in Fig. S5c shows a strong peak for Si-O. Moreover, the specific content of the components was measured by ICP-AES. The content of  $\text{Fe}_2\text{O}_3$  and  $\text{SiO}_2$  was 19.1% and 54% respectively.

### 3.2. Excellent photo-Fenton performance of MM-Fe-Si-PC at low concentrations of $\text{H}_2\text{O}_2$

The photo-Fenton catalytic activity of MM-Fe-Si-PC was investigated at different  $\text{H}_2\text{O}_2$  concentrations under visible light irradiation. The results are presented in Fig. 3a. As shown in the figure, there is almost no degradation of MO without  $\text{H}_2\text{O}_2$ . However, with only 0.2 mM of  $\text{H}_2\text{O}_2$ , 80% of MO is degraded within 30 min, indicating that  $\text{H}_2\text{O}_2$  is an essential factor for the degradation of MO. With increasing concentrations of  $\text{H}_2\text{O}_2$  from 0.2 to 0.4 mM, the degradation efficiency of MO went up from 80% to 97% in 30 min. The enhancement of the degradation rate by addition of  $\text{H}_2\text{O}_2$  is a result of the increase in  $\cdot\text{OH}$  radicals. However, it should be pointed out that when the concentration of  $\text{H}_2\text{O}_2$  was increased from 0.4 to 1.0 mM, the degradation rate of MO was not enhanced any further, and the higher dosages of  $\text{H}_2\text{O}_2$  led to even slight decreases in the degradation rate during the first 15 min, a phenomenon which has been previously observed by many researchers [28,33–35]. The excess  $\text{H}_2\text{O}_2$  reacts with hydroxyl radicals leading to its consumption, thus causing an unwanted scavenging effect as made explicit by the equation below [36].



Hence, a dosage of 0.4 mM  $\text{H}_2\text{O}_2$  is optimal for the degradation of MO. This  $\text{H}_2\text{O}_2$  concentration is really remarkable and is 2.5–112 times lower than the concentration of similar photo-Fenton materials reported in the literature (Table S2 in the Supporting Information). This low concentration of  $\text{H}_2\text{O}_2$  which can still obtain high degradation efficiencies has the potential to lead to a significant reduction in the cost of the photo-Fenton process.

The degradation performance of MM-Fe-Si-PC under this  $\text{H}_2\text{O}_2$  concentration without visible light irradiation was also investigated. As

shown in Fig. 3a, in the absence of visible light, the decrease in MO concentration reaches a steady state in 5 min and then remains unchanged. Thus, light irradiation and  $\text{H}_2\text{O}_2$  are both essential for MO degradation with MM-Fe-Si-PC as the catalyst. The fact that visible light in the presence of MM-Fe-Si-PC and  $\text{H}_2\text{O}_2$  greatly increases the degradation rate of MO demonstrates that MM-Fe-Si-PC is an efficient photo-Fenton catalyst.

The photocatalytic activities of  $\text{Fe}_2\text{O}_3$ - $\text{SiO}_2$  composite samples of different pore types were compared in order to clarify the effect of the hierarchical structure. The MM-Fe-Si-PC material obviously exhibits a higher degradation percentage for MO than Ma-Fe-Si-PC, which possesses only a macroporous structure, or Me-Fe-Si with only a mesoporous structure (Fig. 3b). These observations strongly suggest that the building of the hierarchical macro-mesoporous structure significantly enhances the photo-Fenton catalytic ability of the MM-Fe-Si-PC catalyst.

We also compared the photo-Fenton activity of the MM-Fe-Si-PC sample with commercial  $\text{Fe}_2\text{O}_3$  using a 0.4 mM concentration of  $\text{H}_2\text{O}_2$  (Fig. 3b). Irradiation over time reveals little MO was degraded with  $\text{Fe}_2\text{O}_3$ , indicating that  $\text{Fe}_2\text{O}_3$  cannot respond to such a low concentration of  $\text{H}_2\text{O}_2$ . The control experiment (Fig. 3b) using  $\text{FeCl}_3 \cdot 6\text{H}_2\text{O}$  was also carried out in order to test the catalytic activity of the homogeneous photo-Fenton reaction. The catalytic activity of MM-Fe-Si-PC is slightly better than the homogeneous photo-Fenton system at a  $\text{H}_2\text{O}_2$  concentration of 0.4 mM. Besides, considering that the necessary removal of an iron-containing sludge in the case of the homogeneous photo-Fenton system at the end of the treatment is costly and requires large amount of chemicals and man power, MM-Fe-Si-PC-based heterogeneous photo-Fenton reaction is a better choice. In addition, the resulting solution of the homogeneous photo-Fenton system which contains a large number of  $\text{Fe}^{3+}$  can also cause chroma residue problems (see Fig. S6). With this fact in mind, the treatment of water using MM-Fe-Si-PC ensures not only efficient degradation of MO, but also avoids this chroma residue problem altogether.

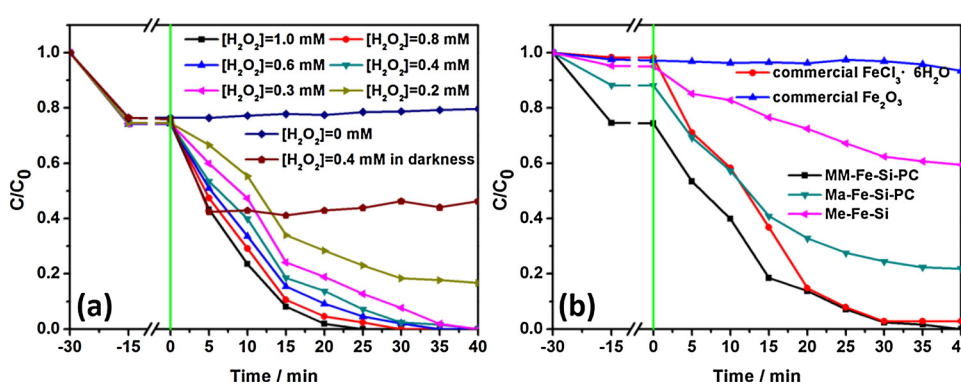


Fig. 3. (a) Photo-Fenton degradation of MO under visible light irradiation of MM-Fe-Si-PC at different  $\text{H}_2\text{O}_2$  concentrations; (b) Photo-Fenton degradation of MO under visible light irradiation of different catalysts at a  $\text{H}_2\text{O}_2$  concentration of 0.4 mM.

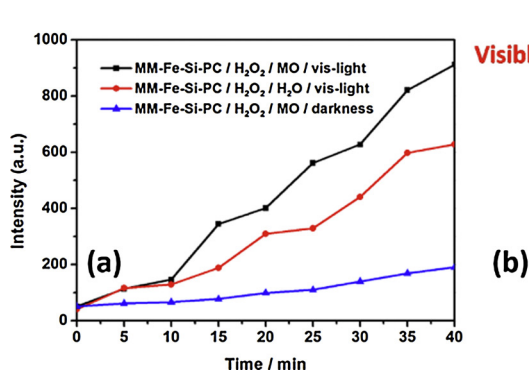
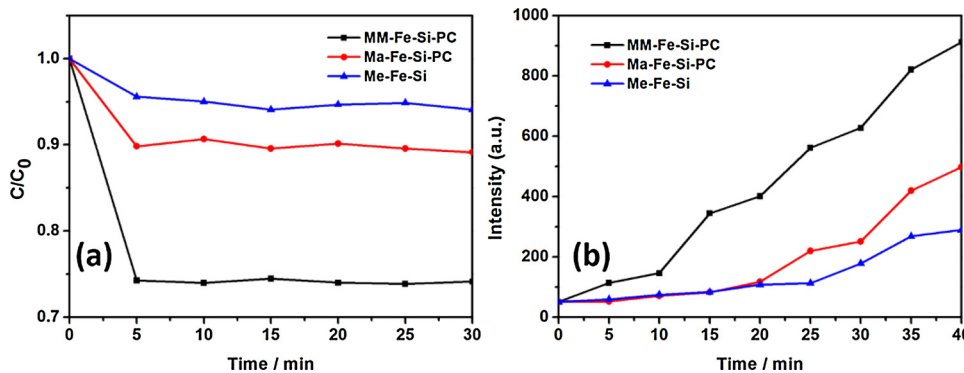


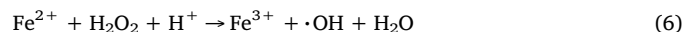
Fig. 4. (a) Changes in PL intensities with light irradiation time for the MM-Fe-Si-PC sample in a 4 mM basic solution of Benzoic acid; (b) Proposed mechanism for the photo-Fenton degradation of MO.



### 3.3. Mechanism for the highly efficient use of H<sub>2</sub>O<sub>2</sub> and high photo-Fenton catalytic activity

The PL technique has been proven to be useful in detecting radical species [37–39], providing essential information for understanding the reaction mechanisms. It has been reported that benzoic acid (BA) can scavenge ·OH radicals to form the fluorescent compound, hydroxybenzoic acid (HBA) [40,41]. We took advantage of this benzoic acid reaction to reveal the reactivity and reaction pathway of the iron species in the MM-Fe-Si-PC catalyst using PL spectroscopy. Fig. 4a presents the PL spectra of the BA solution under various conditions. Usually, the PL intensity is proportional to the amount of hydroxyl radicals produced [42]. As seen in Fig. 4a, in the presence of MO and under visible light irradiation (black line), a strong PL intensity appears over time. Without MO under the same experimental conditions (red line), the PL intensity is obviously lower, indicating the production of ·OH radicals is less. For further comparison, an identical experiment in the dark was conducted with MO and H<sub>2</sub>O<sub>2</sub>, and the data shows a much lower increase in the PL intensity, suggesting dramatically decreased production of ·OH. These results serve as evidence that MO and visible light irradiation act synergistically in enhancing the generation of ·OH radicals, leading to the accelerated Fenton degradation of MO. Based on these results and the previous reports of the photo-Fenton degradation of dyes, a probable photo-Fenton degradation mechanism under visible light irradiation is proposed in Fig. 4b. First, MO is excited by visible light and then transfers electrons to the Fe<sup>3+</sup> in the catalyst to form Fe<sup>2+</sup>. Subsequently, the generated Fe<sup>2+</sup> ions react with H<sub>2</sub>O<sub>2</sub> to produce ·OH radicals which can oxidize the organic dye. Different from the traditional homogeneous or heterogeneous Fenton systems, which usually generate ·OH radicals catalytically by oxidation of Fe<sup>2+</sup> to Fe<sup>3+</sup> followed by reduction back to Fe<sup>2+</sup> by another molecule of H<sub>2</sub>O<sub>2</sub> as shown in Eqs. 3–5, in the MM-Fe-Si-PC system, the excited dye molecules assist the conversion of Fe<sup>3+</sup> to Fe<sup>2+</sup>. Thus, the consumption of H<sub>2</sub>O<sub>2</sub> can be reduced to some extent. In addition, while the conversion of Fe<sup>3+</sup> to Fe<sup>2+</sup> by reacting with H<sub>2</sub>O<sub>2</sub> is relatively slow, the MO-assisted Fe<sup>2+/3+</sup> cycling is quicker, a feature which also leads to higher

degradation rates.



Based on the above mechanism, the three dimensional interconnected pore system of MM-Fe-Si-PC is very beneficial in promoting the efficient use of H<sub>2</sub>O<sub>2</sub> and improving the catalytic activity. MM-Fe-Si-PC possesses abundant worm-like mesopores and well interconnected periodic macropores. Compared with Ma-Fe-Si-PC with only its macropores, MM-Fe-Si-PC has higher specific surface areas (Table S3). On the other hand, in comparison with Me-Fe-Si that only has mesopores, MM-Fe-Si-PC has shorter mesopore channels and more pore openings, leading to the significant increase in the accessible surface area for the diffusing species (i.e., MO) [43]. As a result, MM-Fe-Si-PC exhibits a much better adsorption ability than either Ma-Fe-Si-PC or Me-Fe-Si, as shown in Fig. 5a. Its large and efficient adsorption capacity increases the contact of MO with the active sites on the surface. When MO is excited by visible light, electron-transfer from the excited MO molecules to Fe<sup>3+</sup> is promoted, leading to the formation of Fe<sup>2+</sup>. In addition, the three dimensional macro-mesoporous structure is also beneficial for the diffusion of H<sub>2</sub>O<sub>2</sub>, facilitating the reaction of Fe<sup>2+</sup> with H<sub>2</sub>O<sub>2</sub> and the production of more ·OH radicals. To further confirm this hypothesis, the hydroxyl radical production under visible light irradiation with the different samples was measured. Fig. 5b shows the changes in PL intensity of the samples in BA solutions under irradiation over time. It can be easily seen that the PL intensity increases with the irradiation time, indicating the formation of hydroxyl radicals. The formation rate of ·OH radicals in the case of MM-Fe-Si-PC is the highest, an observation which is consistent with the adsorption performance (Fig. 5a) and the catalytic activity (Fig. 3b).

In addition to the excellent adsorption ability and improved mass transfer, another fact also contributes greatly to the high photo-Fenton catalytic activity – the highly ordered inverse opal structure, which brings out the special photo-physical properties of the catalyst. Fig. 6a

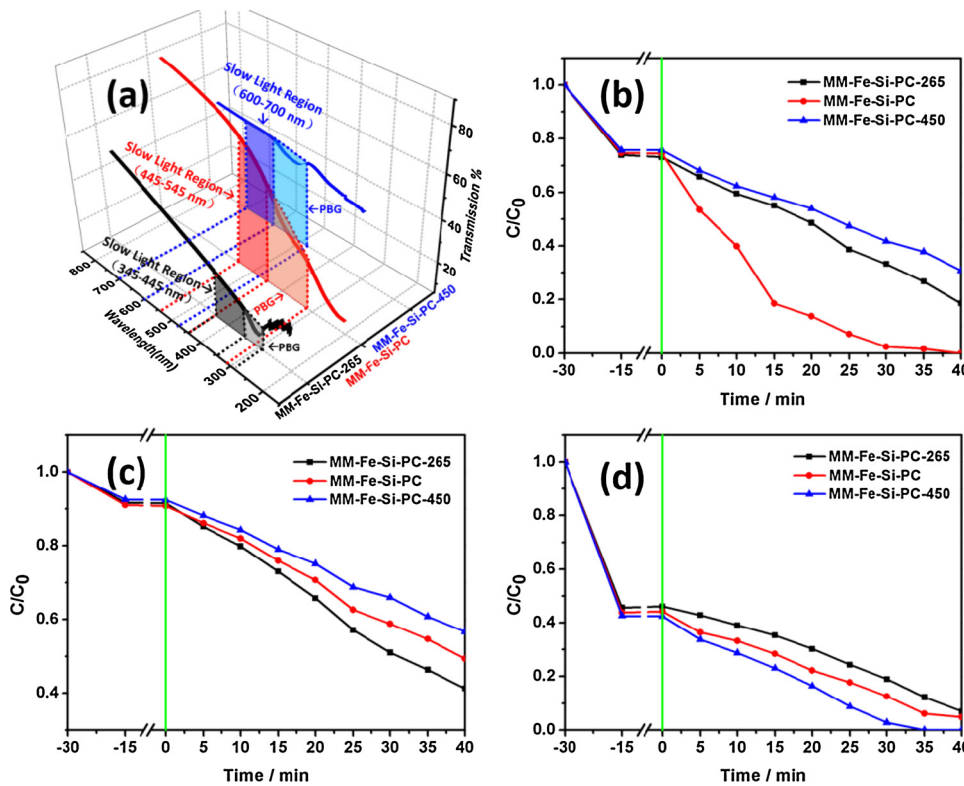


Fig. 6. (a) Transmission spectra of MM-Fe-Si-PC-265, MM-Fe-Si-PC and MM-Fe-Si-PC-450; (b) Photo-Fenton degradation of MO under visible light irradiation of different catalysts at a  $\text{H}_2\text{O}_2$  concentration of 0.4 mM; (c) Photo-Fenton degradation of Coumarin under visible light irradiation of different catalysts at a  $\text{H}_2\text{O}_2$  concentration of 0.4 mM; (d) Photo-Fenton degradation of MB under visible light irradiation of different catalysts at a  $\text{H}_2\text{O}_2$  concentration of 0.4 mM.

shows the transmission spectra of MM-Fe-Si-PC. From the spectra, we can observe a valley from 310 to 445 nm. This transmission valley is attributed to the photonic stop bands (PBG) of the highly ordered inverse opal structure [25,44]. The PBG is a characteristic of the photonic crystal. At the wavelengths corresponding to the edges of these stopbands, photons propagate with strongly reduced group velocity; hence they are called “slow photons”. If the energy of the slow photons overlaps with the absorbance of the material or the dye, the absorption can be enhanced as a result of the increased effective optical path length. For the as-prepared MM-Fe-Si-PC (using PS colloidal crystals with a particle size of 355 nm as the template), the slow-light region is in the vicinity of 500 nm at the edge of the PBG as indicated in Fig. 6a, covering the maximum absorption peak (505 nm) of the MO dye (see Fig. S7b). Therefore, improvement in light-harvesting can be achieved by the slow-light effect, which enhances the excitation of the dyes adsorbed on the catalyst, promoting electron transfer from the excited dyes to  $\text{Fe}^{3+}$ . For comparison, the control samples of MM-Fe-Si-PC-265 and MM-Fe-Si-PC-450 were prepared using PS colloidal crystals with a particle size of 265 and 450 nm as the template. Differently, the valley of PBG is from 295 to 345 nm, and the slow-light-effect region is in the vicinity of 395 nm at the edge of the PBG in MM-Fe-Si-PC-265; the valley of PBG is from 480 to 600 nm, and the slow-light-effect region is in the vicinity of 650 nm at the edge of the PBG in MM-Fe-Si-PC-450 from Fig. 6a. Therefore, the slow-light-effect regions of the two control samples have little overlap with the light absorption of MO. Fig. 6b shows the photo-Fenton catalytic degradation of MO over different samples. Obviously, the degradation efficiency of MM-Fe-Si-PC-265 and MM-Fe-Si-PC-450 to MO were not as high as MM-Fe-Si-PC. Since the adsorption of MO on the three samples were almost the same which can be observed from the 30 min’s dark adsorption data in the figure, the slow-light-effect should be the main reason for the much higher catalytic activity of MM-Fe-Si-PC, demonstrating the slow-light-effect plays a great role during the photo-Fenton reaction.

Further, we did the photo-Fenton degradation experiments on another two dyes—Coumarin and MB, using the three samples with different slow light regions. The maximum absorption peaks of Coumarin

is located at 408 and 428 nm (Fig. S7a) which is in the slow light region of MM-Fe-Si-PC-265; and the maximum absorption peak of MB is located at 664 nm (Fig. S7c) which is belong to the slow light region of MM-Fe-Si-PC-450. The degradation results of Coumarin and MB are shown in Fig. 6c and d, respectively. Obviously, MM-Fe-Si-PC-265 shows the best catalytic activity for the degradation of Coumarin and MM-Fe-Si-PC-450 shows the best catalytic activity for the degradation of MB. These results manifest that, by deliberately tuning the slow-light-effect region of the hierarchical  $\text{Fe}_2\text{O}_3$ - $\text{SiO}_2$  photonic crystal to overlap with the light absorption of different dyes, the catalyst can have highly efficient photo-Fenton catalytic activity for the degradation of a variety of different dyes. In addition, this can be realized by simply adjusting the particles size of the PS template during the preparation process.

#### 3.4. Reusability

The stability and recyclability of catalysts are important considerations for practical applications. Therefore, cycling experiments for the photo-Fenton-mediated degradation of MO with MM-Fe-Si-PC were performed. At the end of each run, the solid catalyst was centrifuged and oven-dried at 70 °C overnight, and then re-introduced into the quartz glass tube for the next experiment. Fig. 7a illustrates the relationship between the MO removal ratio ( $\text{C}/\text{C}_0$ ) and cycling times. After five repeated runs, the MO removal ratio still remains high. The TEM image of the sample in Fig. 7b shows that the hierarchical macromesoporous structure still is maintained after five runs. In addition, the XRD pattern of MM-Fe-Si-PC after 5 runs have also been taken as shown in Fig. S8. Two typical peaks at 33.0° and 55.2° corresponding to the (222) and (440) planes of  $\text{Fe}_2\text{O}_3$  can be obviously observed, which is almost the same with those in Fig. 2a from the sample before catalytic reactions, indicating the chemical constitution of the photonic crystals remains stable in the photo-Fenton reaction. Furthermore, the leaching of iron ions during the reaction process was measured by inductively coupled plasma mass spectrometry (ICP-MS). The results tell that the leaching of iron ions remained below 0.40 ppm in all the cycles (see

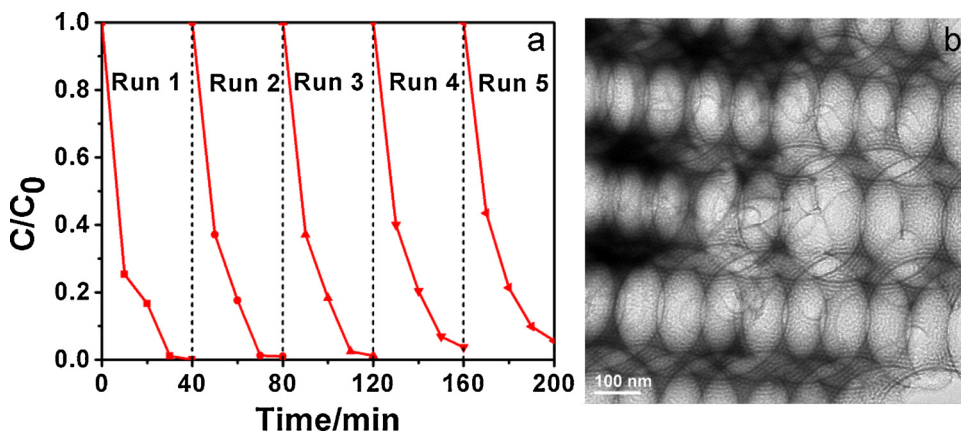


Table S4), further demonstrating that the hierarchical macro-mesoporous  $\text{Fe}_2\text{O}_3\text{-SiO}_2$  photonic crystal is stable and can be used repeatedly.

#### 4. Conclusions

$\text{Fe}_2\text{O}_3\text{-SiO}_2$  photonic crystals with hierarchically structured macro-mesopores have been developed for treating dye-contaminated wastewater by a photo-Fenton mechanism. A remarkably high and stable photo-Fenton performance for removal of MO was achieved using a very low concentration of  $\text{H}_2\text{O}_2$  under visible light illumination. The efficient utilization of  $\text{H}_2\text{O}_2$  and the high catalytic activity of MM-Fe-Si-PC can be ascribed to the high accessible surface area of hierarchical macro-mesoporous structure and the slow-light effect of the photonic crystal. The efficient utilization of  $\text{H}_2\text{O}_2$  can lead to a significant reduction in the costs associated with the photo-Fenton process when applied at the industrial scale. In addition, it is experimentally demonstrated that by deliberately tuning the slow-light-effect region of the catalyst, it can be effective photo-Fenton catalyst for degradation of a variety of dyes. The configuration of the catalyst in this work represents a new and promising strategy for the development of other highly efficient photo-Fenton catalyst.

#### Acknowledgements

This work was financially supported by National Nature Science Foundation of China (21777044, 21407049, 21237003 and 21377038), China Postdoctoral Science Foundation (2015T80409), the Science and Technology Commission of Shanghai Municipality (16JC1401400), and the Science and Technology Commission of Jiangsu Province (BC2015135).

#### Appendix A. Supplementary data

Supplementary data associated with this article can be found, in the online version, at <http://dx.doi.org/10.1016/j.apcatb.2017.08.039>.

#### References

- S. Sansuk, S. Srijaranai, S. Srijaranai, A new approach for removing anionic organic dyes from wastewater based on electrostatically driven assembly, *Environ. Sci. Technol.* 50 (2016) 6477–6484.
- S.S. Lee, H. Bai, Z. Liu, D.D. Sun, Novel-structured electrospun  $\text{TiO}_2\text{/CuO}$  composite nanofibers for high efficient photocatalytic cogeneration of clean water and energy from dye wastewater, *Water Res.* 47 (2013) 4059–4073.
- T. Jiao, H. Zhao, J. Zhou, Q. Zhang, X. Luo, J. Hu, Q. Peng, X. Yan, Self-assembly reduced graphene oxide nanosheet hydrogel fabrication by anchorage of chitosan/silver and its potential efficient application toward dye degradation for wastewater treatments, *ACS Sustain. Chem. Eng.* 3 (2015) 3130–3139.
- L.I. Doumic, P.A. Soares, M.A. Ayude, M. Cassanello, R.A.R. Boaventura, V.J.P. Vilar, Enhancement of a solar photo-Fenton reaction by using ferrioxalate complexes for the treatment of a synthetic cotton-textile dyeing wastewater, *Chem. Eng. J.* 277 (2015) 86–96.
- Y.-Y. Bai, Y. Lu, J.-K. Liu, An efficient photocatalyst for degradation of various organic dyes:  $\text{ag@Ag}_2\text{MoO}_4\text{-AgBr}$  composite, *J. Hazard. Mater.* 307 (2016) 26–35.
- W.-D. Oh, Z. Dong, T.-T. Lim, Generation of sulfate radical through heterogeneous catalysis for organic contaminants removal: current development, challenges and prospects, *Appl. Catal. B: Environ.* 194 (2016) 169–201.
- X. Yang, H. Sun, L. Zhang, L. Zhao, J. Lian, Q. Jiang, High efficient photo-Fenton catalyst of  $\alpha\text{-Fe}_2\text{O}_3\text{/MoS}_2$  hierarchical nanoheterostructures: reutilization for supercapacitors, *Sci. Rep.* 6 (2016) 31591.
- Z.-M. Cui, J. Hao, J. Liu, W.-G. Song, Mesoporous silica coating on hierarchical flowerlike  $\text{Fe}_2\text{O}_3$  with enhanced catalytic activity for Fenton-like reaction, *RSC Adv.* 6 (2016) 74545–74549.
- K. Li, Y. Zhao, M.J. Janik, C. Song, X. Guo, Facile preparation of magnetic mesoporous  $\text{Fe}_3\text{O}_4\text{/C/Cu}$  composites as high performance Fenton-like catalysts, *Appl. Surf. Sci.* 396 (2017) 1383–1392.
- Y. Zhang, C. Liu, B. Xu, F. Qi, W. Chu, Degradation of benzotriazole by a novel Fenton-like reaction with mesoporous  $\text{Cu/MnO}_2$ : Combination of adsorption and catalysis oxidation, *Appl. Catal. B: Environ.* 199 (2016) 447–457.
- Y. Liu, W. Jin, Y. Zhao, G. Zhang, W. Zhang, Enhanced catalytic degradation of methylene blue by  $\alpha\text{-Fe}_2\text{O}_3$ /graphene oxide via heterogeneous photo-Fenton reactions, *Appl. Catal. B: Environ.* 206 (2017) 642–652.
- N. Wang, Y. Du, W. Ma, P. Xu, X. Han, Rational design and synthesis of  $\text{SnO}_2$ -encapsulated  $\alpha\text{-Fe}_2\text{O}_3$  nanocubes as a robust and stable photo-Fenton catalyst, *Appl. Catal. B: Environ.* 210 (2017) 23–33.
- S. Chou, C. Huang, Application of a supported iron oxyhydroxide catalyst in oxidation of benzoic acid by hydrogen peroxide, *Chemosphere* 38 (1999) 2719–2731.
- H. Cheng, S. Chou, S. Chen, C. Yu, Photoassisted Fenton degradation of phthalocyanine dyes from wastewater of printing industry using  $\text{Fe(II)}/\gamma\text{-Al}_2\text{O}_3$  catalyst in up-flow fluidized-bed, *J. Environ. Sci.* 26 (2014) 1307–1312.
- M.L. Rache, A.R. García, H.R. Zea, A.M.T. Silva, L.M. Madeira, J.H. Ramírez, Azo-dye orange II degradation by the heterogeneous Fenton-like process using a zeolite Y-Fe catalyst—kinetics with a model based on the Fermi's equation, *Appl. Catal. B: Environ.* 146 (2014) 192–200.
- P.P. Gan, S.F.Y. Li, Efficient removal of Rhodamine B using a rice hull-based silica supported iron catalyst by Fenton-like process, *Chem. Eng. J.* 229 (2013) 351–363.
- N.A. Zubir, C. Yacou, J. Motuzas, X. Zhang, J.C. Diniz da Costa, Structural and functional investigation of graphene oxide- $\text{Fe}_3\text{O}_4$  nanocomposites for the heterogeneous Fenton-like reaction, *Sci. Rep.* 4 (2014) 4594.
- A. Babuponnu, K. Muthukumar, A review on Fenton and improvements to the Fenton process for wastewater treatment, *J. Environ. Chem. Eng.* 2 (2014) 557–572.
- T.T. Vu, G. Marbán, Sacrificial template synthesis of high surface area metal oxides. Example: an excellent structured Fenton-like catalyst, *Appl. Catal. B: Environ.* 152–153 (2014) 51–58.
- X. Zheng, D. Li, X. Li, J. Chen, C. Cao, J. Fang, J. Wang, Y. He, Y. Zheng, Construction of  $\text{ZnO}/\text{TiO}_2$  photonic crystal heterostructures for enhanced photocatalytic properties, *Appl. Catal. B: Environ.* 168–169 (2015) 408–415.
- X. Li, J. Yu, M. Jaroniec, Hierarchical photocatalysts, *Chem. Soc. Rev.* 45 (2016) 2603–2636.
- T.K. Rahul, N. Sandhyarani, Nitrogen-fluorine co-doped titania inverse opals for enhanced solar light driven photocatalysis, *Nanoscale* 7 (2015) 18259–18270.
- F. Sordello, C. Miner, Photocatalytic hydrogen production on Pt-loaded  $\text{TiO}_2$  inverse opals, *Appl. Catal. B: Environ.* 163 (2015) 452–458.
- L. Lu, F. Teng, SenTapas, D. Qi, L. Wang, J. Zhang, Synthesis of visible-light driven  $\text{Cr}_x\text{O}_y\text{/TiO}_2$  binary photocatalyst based on hierarchical macro-mesoporous silica, *Appl. Catal. B: Environ.* 163 (2015) 9–15.
- D. Qi, L. Lu, Z. Xi, L. Wang, J. Zhang, Enhanced photocatalytic performance of  $\text{TiO}_2$  based on synergistic effect of  $\text{Ti}_3^+$  self-doping and slow light effect, *Appl. Catal. B: Environ.* 160–161 (2014) 621–628.
- D. Qi, L. Lu, L. Wang, J. Zhang, Improved SERS sensitivity on plasmon-free  $\text{TiO}_2$  photonic microarray by enhancing light-matter coupling, *J. Am. Chem. Soc.* 136 (2014) 9886–9889.
- H.-x. Zhong, J. Wang, Y.-w. Zhang, W.-l. Xu, W. Xing, D. Xu, Y.-f. Zhang, X.-b.

Zhang, ZIF-8 derived graphene-based nitrogen-doped porous carbon sheets as highly efficient and durable oxygen reduction electrocatalysts, *Angew. Chem. Int. Ed.* 53 (2014) 14235–14239.

[28] X. Zhang, Y. Ding, H. Tang, X. Han, L. Zhu, N. Wang, Degradation of bisphenol A by hydrogen peroxide activated with CuFeO<sub>2</sub> microparticles as a heterogeneous Fenton-like catalyst: efficiency, stability and mechanism, *Chem. Eng. J.* 236 (2014) 251–262.

[29] Y. Zhang, M. Yu, C. Zhang, Y. Wang, Y. Di, C. Wang, H. Lu, Highly specific enrichment of N-glycoproteome through a nonreductive amination reaction using Fe 3 O 4@ SiO<sub>2</sub>-aniline nanoparticles, *Chem. Commun.* 51 (2015) 5982–5985.

[30] C. Gong, D. Chen, X. Jiao, Q. Wang, Continuous hollow [small alpha]-Fe<sub>2</sub>O<sub>3</sub> and [small alpha]-Fe fibers prepared by the sol-gel method, *J. Mater. Chem.* 12 (2002) 1844–1847.

[31] X.-F. Lu, X.-Y. Chen, W. Zhou, Y.-X. Tong, G.-R. Li,  $\alpha$ -Fe<sub>2</sub>O<sub>3</sub>@ PANI core-shell nanowire arrays as negative electrodes for asymmetric supercapacitors, *ACS Appl. Mater. Interfaces* 7 (2015) 14843–14850.

[32] L. Wang, H. Yang, X. Liu, R. Zeng, M. Li, Y. Huang, X. Hu, Constructing hierarchical tectorium-like  $\alpha$ -Fe<sub>2</sub>O<sub>3</sub>/PPy nanoarrays on carbon cloth for solid-state asymmetric supercapacitors, *Angewandte Chemie* 129 (2017) 1125–1130.

[33] A.N. Soon, B. Hameed, Degradation of Acid Blue 29 in visible light radiation using iron modified mesoporous silica as heterogeneous Photo-Fenton catalyst, *Appl. Catal. A: Gen.* 450 (2013) 96–105.

[34] C. Bouasla, M.E.-H. Samar, F. Ismail, Degradation of methyl violet 6B dye by the Fenton process, *Desalination* 254 (2010) 35–41.

[35] N. Panda, H. Sahoo, S. Mohapatra, Decolorization of methyl orange using fenton-like mesoporous Fe 2 O 3-SiO<sub>2</sub> composite, *J. Hazard. Mater.* 185 (2011) 359–365.

[36] J. Du, J. Bao, X. Fu, C. Lu, S.H. Kim, Mesoporous sulfur-modified iron oxide as an effective Fenton-like catalyst for degradation of bisphenol A, *Appl. Catal. B: Environ.* 184 (2016) 132–141.

[37] J. Yu, G. Dai, B. Cheng, Effect of crystallization methods on morphology and photocatalytic activity of anodized TiO<sub>2</sub> nanotube array films, *J. Phys. Chem. C* 114 (2010) 19378–19385.

[38] K.-I. Ishibashi, A. Fujishima, T. Watanabe, K. Hashimoto, Detection of active oxidative species in TiO<sub>2</sub> photocatalysis using the fluorescence technique, *Electrochem. Commun.* 2 (2000) 207–210.

[39] S. Guo, G. Zhang, Green synthesis of a bifunctional Fe-montmorillonite composite during the Fenton degradation process and its enhanced adsorption and heterogeneous photo-Fenton catalytic properties, *RSC Adv.* 6 (2016) 2537–2545.

[40] M. Xing, J. Zhang, B. Qiu, B. Tian, M. Anpo, M. Che, A brown mesoporous TiO<sub>2-x</sub>/MCF composite with an extremely high quantum yield of solar energy photocatalysis for H<sub>2</sub> evolution, *Small* 11 (2015) 1920–1929.

[41] C. Sánchez-Moreno, Review Methods used to evaluate the free radical scavenging activity in foods and biological systems, *Food Sci. Technol. Int.* 8 (2002) 121–137.

[42] S. Sakhivel, H. Kisch, Daylight photocatalysis by carbon-modified titanium dioxide, *Angew. Chem. Int. Ed.* 42 (2003) 4908–4911.

[43] J. Du, X. Lai, N. Yang, J. Zhai, D. Kisailus, F. Su, D. Wang, L. Jiang, Hierarchically ordered macro- mesoporous TiO<sub>2</sub>-graphene composite films: improved mass transfer, reduced charge recombination, and their enhanced photocatalytic activities, *ACS Nano* 5 (2010) 590–596.

[44] X. Chen, J. Ye, S. Ouyang, T. Kako, Z. Li, Z. Zou, Enhanced incident photon-to-electron conversion efficiency of tungsten trioxide photoanodes based on 3D-photonic crystal design, *ACS Nano* 5 (2011) 4310–4318.